



Neutral Iron Emission Lines from the Dayside of KELT-9b: The GAPS Program with HARPS-N at TNG XX

Lorenzo Pino¹ , Jean-Michel Désert¹, Matteo Brogi^{2,3,4} , Luca Malavolta^{5,6} , Aurélien Wyttenbach⁷, Michael Line⁸ , Jens Hoeijmakers^{9,10}, Luca Fossati¹¹ , Aldo Stefano Bonomo³ , Valerio Nascimbeni¹², Vatsal Panwar¹, Laura Affer¹³, Serena Benatti¹³, Katia Biazzo⁶ , Andrea Bignamini¹⁴, Francesco Borsa¹⁵, Ilaria Carleo^{12,16} , Riccardo Claudi¹², Rosario Cosentino¹⁷, Elvira Covino¹⁸ , Mario Damasso³, Silvano Desidera¹², Paolo Giacobbe³, Avet Harutyunyan¹⁷, Antonino Francesco Lanza⁶ , Giuseppe Leto⁶ , Antonio Maggio¹³ , Jesus Maldonado¹³ , Luigi Mancini^{3,19,20} , Giuseppina Micela¹³, Emilio Molinari²¹ , Isabella Pagano⁶ , Giampaolo Piotto⁵ , Ennio Poretti^{15,17} , Monica Rainer²² , Gaetano Scandariato⁶, Alessandro Sozzetti³ , Romain Allart¹⁰, Luca Borsato⁵, Giovanni Bruno⁶, Luca Di Fabrizio¹⁷, David Ehrenreich¹⁰ , Aldo Fiorenzano¹⁷, Giuseppe Frustagli^{15,23}, Baptiste Lavie¹⁰ , Christophe Lovis¹⁰, Antonio Magazzù¹⁷, Domenico Nardiello⁵ , Marco Pedani¹⁷, and Riccardo Smareglia¹⁴

¹ Anton Pannekoek Institute for Astronomy, University of Amsterdam, Science Park 904, 1098 XH Amsterdam, The Netherlands; l.pino@uva.nl

² Department of Physics, University of Warwick, Coventry CV4 7AL, UK

³ INAF—Osservatorio Astrofisico di Torino, Via Osservatorio 20, I-10025 Pino Torinese, Italy

⁴ Centre for Exoplanets and Habitability, University of Warwick, Gibbet Hill Road, Coventry CV4 7AL, UK

⁵ Dipartimento di Fisica e Astronomia “Galileo Galilei,” Università di Padova, Vicolo dell’Osservatorio 3, I-35122 Padova, Italy

⁶ INAF—Osservatorio Astrofisico di Catania, Via S. Sofia 78, I-95123 Catania, Italy

⁷ Leiden Observatory, Leiden University, Postbus 9513, 2300 RA Leiden, The Netherlands

⁸ Arizona State University, Tempe, AZ, USA

⁹ University of Bern, Center for Space and Habitability, Gesellschaftsstrasse 6, CH-3012 Bern, Switzerland

¹⁰ Observatoire astronomique de l’Université de Genève, 51 Chemin des Maillettes, 1290 Versoix, Switzerland

¹¹ Space Research Institute, Austrian Academy of Sciences, Schmiedlstrasse 6, A-8041 Graz, Austria

¹² INAF—Osservatorio Astronomico di Padova, Vicolo dell’Osservatorio 5, I-35122 Padova, Italy

¹³ INAF—Osservatorio Astronomico di Palermo, Piazza del Parlamento, 1, I-90134 Palermo, Italy

¹⁴ INAF—Osservatorio Astronomico di Trieste, Via Tiepolo 11, I-34143 Trieste, Italy

¹⁵ INAF—Osservatorio Astronomico di Brera, Via E. Bianchi 46, I-23807 Merate, Italy

¹⁶ Astronomy Department and Van Vleck Observatory, Wesleyan University, Middletown, CT 06459, USA

¹⁷ Fundación Galileo Galilei-IAF, Rambla José Ana Fernández Pérez 7, E-38712 Breña Baja, TF, Spain

¹⁸ INAF—Osservatorio Astronomico di Capodimonte, Salita Moiariello 16, I-80131 Napoli, Italy

¹⁹ Department of Physics, University of Rome Tor Vergata, Via della Ricerca Scientifica 1, I-00133 Rome, Italy

²⁰ Max Planck Institute for Astronomy, Königstuhl 17, D-69117 Heidelberg, Germany

²¹ INAF Osservatorio Astronomico di Cagliari & REM, Via della Scienza, 5, I-09047 Selargius CA, Italy

²² INAF-Osservatorio Astrofisico di Arcetri, Largo Enrico Fermi 5, I-50125 Firenze, Italy

²³ Dipartimento di Fisica G. Occhialini, Università degli Studi di Milano-Bicocca, Piazza della Scienza 3, I-20126 Milano, Italy

Received 2019 November 19; revised 2020 April 8; accepted 2020 April 22; published 2020 May 14

Abstract

We present the first detection of atomic emission lines from the atmosphere of an exoplanet. We detect neutral iron lines from the dayside of KELT-9b ($T_{\text{eq}} \sim 4000$ K). We combined thousands of spectrally resolved lines observed during one night with the HARPS-N spectrograph ($R \sim 115,000$), mounted at the Telescopio Nazionale Galileo. We introduce a novel statistical approach to extract the planetary parameters from the binary mask cross-correlation analysis. We also adapt the concept of contribution function to the context of high spectral resolution observations, to identify the location in the planetary atmosphere where the detected emission originates. The average planetary line profile intersected by a stellar G2 binary mask was found in emission with a contrast of 84 ± 14 ppm relative to the planetary plus stellar continuum ($40\% \pm 5\%$ relative to the planetary continuum only). This result unambiguously indicates the presence of an atmospheric thermal inversion. Finally, assuming a modeled temperature profile previously published, we show that an iron abundance consistent with a few times the stellar value explains the data well. In this scenario, the iron emission originates at the 10^{-3} – 10^{-5} bar level.

Unified Astronomy Thesaurus concepts: [Exoplanet atmospheres \(487\)](#); [Exoplanet atmospheric composition \(2021\)](#); [High resolution spectroscopy \(2096\)](#)

1. Introduction

Ultra-hot Jupiters are tidally locked gaseous giant planets that orbit their host stars in mere hours or days, often reaching temperatures above 2500 K in their permanent daysides. Unlike for their cooler counterparts, equilibrium chemistry should provide an accurate description of their chemical network, and known condensates are likely secluded to their nightside (Kitzmann et al. 2018; Lothringer et al. 2018; Parmentier et al. 2018; Helling et al. 2019).

Detections of atomic metals at the day–night transition of their atmospheres (WASP-12b, Fossati et al. 2010; Haswell et al. 2012; KELT-9b, Hoeijmakers et al. 2018, 2019; Cauley et al. 2019; MASCARA-2b, Casasayas-Barris et al. 2019; WASP-121b, Sing et al. 2019; Gibson et al. 2020) show that heavy elements are not necessarily sequestered deep in the atmospheres of these planets. This may also indicate the presence of a shallow radiative–convective boundary (Thorngren et al. 2019). Iron is an element of particular interest. Indeed, its abundance is a proxy for the

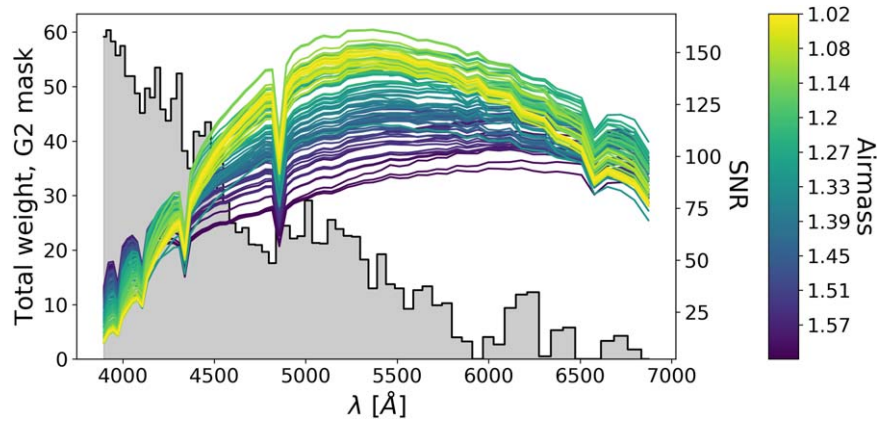


Figure 1. Signal-to-noise ratio as a function of airmass and wavelength (solid curves), and total weight within the mask for each spectral bin (gray histogram; accounting for the number of spectral lines and their depth only). Spectra acquired at lower airmass are expected to have higher signal-to-noise ratio throughout the spectrum, due to a lower optical depth of Earth atmosphere, but the malfunction of the atmospheric dispersion corrector modifies this behavior. This effect is particularly severe in the blue, where most of the information on the planet lies, as quantified by the weight in the binary mask. Indeed, while no changes in observing conditions were noticeable in our run, the bluest orders of the lowest airmass spectra have a signal-to-noise ratio which is half compared to airmass 1.6, the maximum reached within our run.

metallicity of stars, and thus a particularly relevant case for comparison between planetary and stellar metallicity. It was detected both in neutral and ionized form at the day–night transition in the atmosphere of KELT-9b (Hoeijmakers et al. 2018; Borsa et al. 2019; Cauley et al. 2019), probing pressures as low as a few μbar (Hoeijmakers et al. 2019). These lines likely originate within the extended atmosphere of the planet, also detected with $\text{H}\alpha$ and Ca II lines (Yan & Henning 2018; Yan et al. 2019; Turner et al. 2020). Ionized iron was also found in the upper atmosphere of MASCARA-2b (Casasayas-Barris et al. 2019) and in the exospheres of WASP-12b and WASP-121b (Haswell et al. 2012; Sing et al. 2019). Yet, a detection of photospheric planetary iron lines is still lacking.

In this paper we employ the high-resolution ($R \sim 115,000$) spectrograph HARPS-N, mounted at the Telescopio Nazionale Galileo (TNG), to observe for the first time the thermal emission of an exoplanet with this instrument. To do so, we target KELT-9b, monitoring the planet from quadrature to right before it is eclipsed behind the star. We describe our observations and data reduction in Section 2 and Appendix A, including an adaptation of the line-weighted stellar binary masks method, traditionally used to extract radial velocities of exoplanets, to extract the signal of the planet via a cross-correlation function (CCF). We present the results of this analysis in Section 3. We then perform a second analysis of the extracted planetary CCF to derive atmospheric parameters of the planet based on models (Sections 4, 5). To this aim, we introduce a new method to compare models and observations making use of the CCF technique with a line-weighted binary mask, present a novel adaptation of the concept of contribution function to the context of cross-correlation analyses (Section 4), and apply these tools to our observations (Section 5). We discuss the implications of our study in Section 6.

2. Methods: Treatment of Data

2.1. Observations and Data Reduction

We observed the KELT-9 system in the framework of a Long-Term program (PI G. Micela) with HARPS-N and GIANO-B in GIARPS@TNG configuration (Claudi et al. 2017), as part of the GAPS project (Covino et al. 2013). For the present work, we only used the HARPS-N observations taken from the 2018 July 22

21:23 UT to the 2018 July 23 05:21 UT. The GIANO-B observations will be the target of a dedicated study. We collected 89 HARPS-N exposures, each with 180 s of integration. This is shorter than in Hoeijmakers et al. (2018, 2019), who used an exposure time of 600 s. With this choice, the planet moved by at most 2.25 km s^{-1} during each exposure, which smeared the signal over 2.7 pixels. Considering the transit centered at phase 0, the planetary phases covered the range between 0.227 and 0.452, such that the planet was not occulted by the stellar disk.

We extracted and calibrated the spectra using the standard Data Reduction Software (DRS, version 3.7.1; Dumusque 2018). To avoid the increase of correlated noise from data interpolation, we performed our analysis on the individual echelle orders (e2ds spectra), after correcting for the blaze function. As previously reported by Borsa et al. (2019), our observations were affected by a malfunction of the Atmospheric Dispersion Corrector that caused a deformation of the spectral energy distribution due to chromatic losses, and a concomitant loss of efficiency in the blue part of the spectra across the night (see Figure 1). While we mitigated this effect with a custom color-correction, following Malavolta et al. (2017), it is not possible to recover the lost signal-to-noise ratio at shorter wavelengths. We did not correct for telluric lines, because our analysis naturally excludes regions that are contaminated by them (Section 2.2). We then aligned the stellar spectra by removing the Barycentric Earth Radial Velocity motion, effectively shifting the spectra to the barycentric rest-frame of the solar system. This allowed us to build a high signal-to-noise ratio master stellar spectrum by (1) rescaling every order to its average counts value and (2) computing a median in time for each order. The stellar motion induced by the planet amounted to about 0.2 km s^{-1} throughout the night, and did not significantly impact the shape of the stellar lines, which were rotationally broadened by more than 100 km s^{-1} . Since the planet moved in radial velocity by more than one pixel per exposure for most of the night, the resulting master spectrum contained the planetary lines only in minimal part. Each single e2ds spectrum was then divided by the master stellar spectrum, which removed the stellar lines. This procedure effectively provides the planet emission spectrum normalized to the stellar emission spectrum and planet continuum plus 1 (see Appendix A). A high-pass filter was then applied to each of the resulting rows to remove residual discontinuities and low-order

variations due to imprecise blaze or color correction (see Appendix A). We found that the application of the high-pass filter enhanced the precision on the retrieved parameters by a factor of about 2. We finally applied a custom binary mask cross-correlation method (see Section 2.2).

2.2. Line-weighted Binary Mask CCF

With a temperature comparable to a K-dwarf, the atmosphere of KELT-9b should exhibit thousands of optical atomic transitions. The technique of cross-correlation (Baranne et al. 1979; Sparks & Ford 2002; Snellen et al. 2010) is best suited for their search (Hoeijmakers et al. 2019). The technique was applied with different flavors (e.g., template matching, binary mask), and consisted in stacking these thousands of planetary lines to abate the photon noise, which hinders their detection.

We adopted a CCF technique with a weighted binary mask (Baranne et al. 1996; Pepe et al. 2002),²⁴ where weights are attributed to individual spectral lines according to their information content (see Appendix B). It can employ the classic stellar binary masks used in the search of planets with the radial velocity method, as well as custom binary masks, and can be applied both to models and data. Compared to other cross-correlation schemes (Snellen et al. 2010), the binary mask approach preserves the contrast of the lines that it intercepts, which allows the comparison of the strength of different spectral features (Pino et al. 2018a). In practice, our technique extracts the average planet line normalized to the planet plus star continuum (which we call planet excess). This is similar to a least-squares deconvolution scheme (LSD; Donati et al. 1997), but without deconvolving the cross-correlation vector (with no loss of accuracy in the interpretation; Section 4). This average line profile can be used to directly extract observational properties of the planetary emission (Section 3), but the extraction of parameters of the atmospheric structure requires the extra step of model comparison, for which we present a new method (Section 4).

Other works have relied on similar definitions of the CCF (Hoeijmakers et al. 2019). However, they determined the weights on single pixels using model-injection, thus based on their information content, with the aim of reaching the highest signal-to-noise ratio on the planetary detection. In our approach, the binary mask attributes weights to single lines, as opposed to single pixels, with the advantage of reduced complexity and model-dependence. The consequently easier interpretation is obtained at the cost of a possible loss of signal-to-noise ratio, especially in the wings of the lines.

Since the planet has a temperature comparable to that of a star, in this work we adopted standard G2, K0, and K5 stellar masks provided by the DRS, optimized to extract radial velocities for planets orbiting stars for that spectral type. These masks are designed to exclude parts of the spectrum that are contaminated by telluric lines.

The results are mostly independent of the choice of the spectral type of the mask. This is likely because the masks share the strongest lines. Indeed, among the 1000 strongest lines in each mask, the majority of the lines are closer than 0.001 Å, less than one tenth of a pixel. In percentage, the masks share 74.4% (G2 versus K0), 82.6% (G2 versus K5), and

84.4% (K0 versus K5) of the strongest lines. In the following, we discuss the G2 mask case.

A CCF is computed for every exposure. The result is an “exposure matrix” which displays the planet trace in a diagram with radial velocity displacement from the stellar rest frame on the x -axis, and planetary phase (or exposure) on the y -axis (Figure 2, upper panel). The fit (Section 4) was directly performed on this exposure matrix. However, we also display the results in the traditional K_p - v_{sys} diagram, which visually highlights the presence or lack of a signal. In practice, we parameterized the planet orbit with a Keplerian velocity K_p , appropriate for a circular orbit, and moved to the corresponding planet rest frame. Only the correct K_p aligns the individual CCFs, which are then summed. The maximum is thus found at the global radial velocity of the system (systemic velocity, v_{sys}). This is conveniently represented in the K_p - v_{sys} diagram (Figure 2, middle panels).

3. Observational Results

In Figure 2, we present the result of applying a G2 binary mask to the planet-to-star flux ratio. In practice, what we see is the average planet emission line intersected by the G2 binary mask normalized to the planetary and stellar continua. This emission is interpreted as due to the atmosphere of the planet.

The planetary atmospheric spectral feature, as seen through the G2 mask, has a contrast of (84 ± 1) ppm relative to the continuum. We obtained this by fitting a Gaussian curve to the planetary signal integrated over the exposures assuming the best-fit K_p (see Figure 2, lower panel; Section 5.1). The formal error is likely underestimated due to the presence of correlated noise. By replacing the formal error with the standard deviation far from the planet signal (14 ppm, calculated at $-200 \text{ km s}^{-1} < v_{\text{sys}} < -100 \text{ km s}^{-1}$), the signal-to-noise ratio of the detection is 6.

We then assumed that the continuum is the sum of the stellar and planetary continua (see Appendix A). We further assumed that the stellar and planetary continua are blackbodies at temperatures of 10,000 K and 4570 K (Wong et al. 2019), respectively. The contrast relative to the planetary continuum is then

$$\frac{F_{\text{lines p}}}{F_{\text{cont, p}}} = 84 \cdot \left(1 + \frac{F_{\text{cont, s}}}{F_{\text{cont, p}}} \right) \text{ppm}, \quad (1)$$

yielding $(40 \pm 5)\%$.

The planet excess appears in emission and not in absorption, which is an unambiguous sign of the presence of a thermal inversion in the atmosphere of the planet (see Schwarz et al. 2015; Nugroho et al. 2017; Section 6.1).

4. Methods: Extracting Atmospheric Parameters of KELT-9b

The next step is extracting the planetary parameters from the CCF. This requires two ingredients: (1) a parameterized model for the exoplanet atmosphere (Section 4.1) and (2) a cross-correlation to likelihood mapping (Section 4.2). We also adapt the concept of contribution functions to the line-weighted binary mask CCF, to identify the pressure range probed by our analysis (Section 4.3).

²⁴ We do not normalize by the standard deviation. As such, our scheme is a cross-covariance in the statistical sense, but we call it cross-correlation following Baranne et al. (1996) and the signal processing nomenclature.

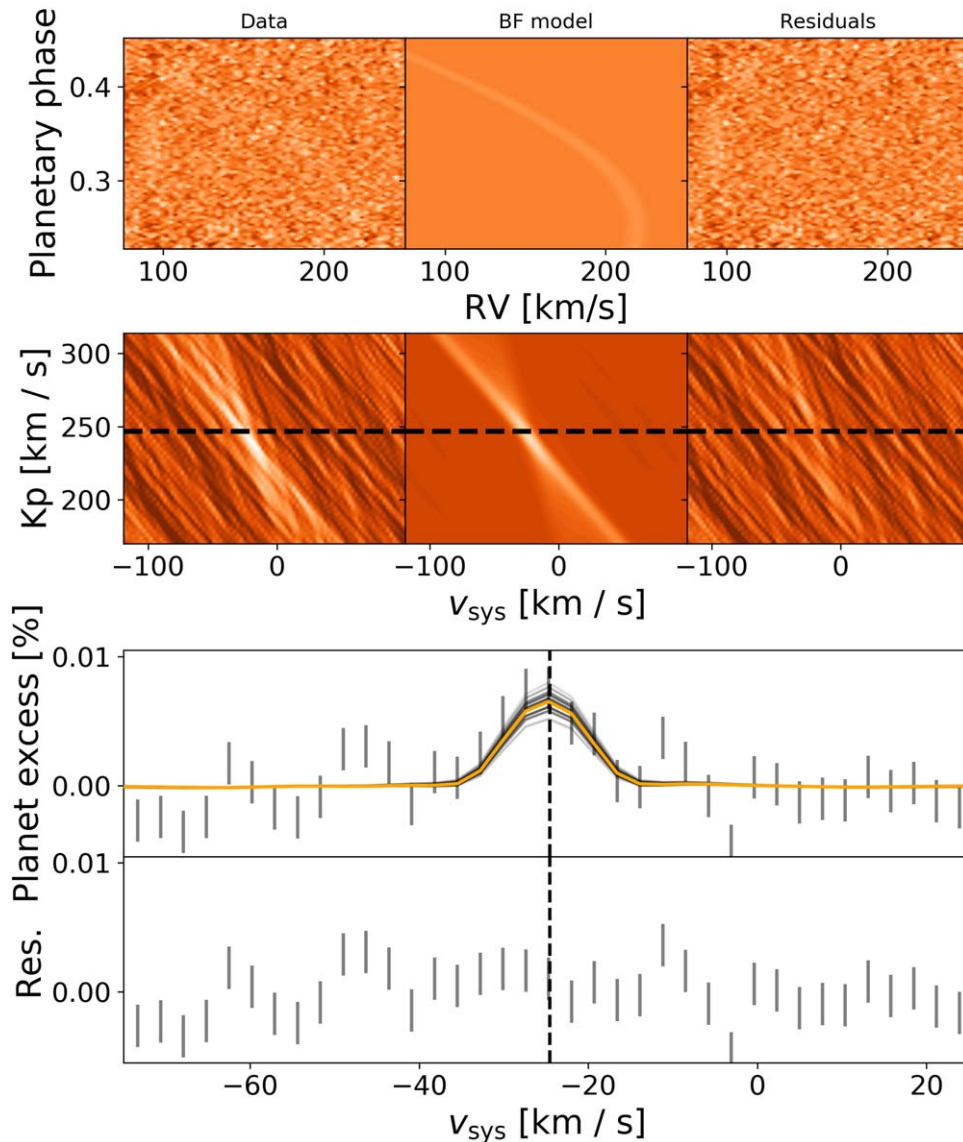


Figure 2. Observed and modeled average planet emission line intersected by the G2 mask, and residuals between data and best-fit model. Upper panel: the exposure matrix in the region where we performed the fit. The curvature of the planetary trace is due to its overnight change in radial velocity compared to its host star. Middle panel: K_p - v_{sys} diagram for data, best-fit model, and residuals. The color scale is the same across the three panels, showing that the residuals map is clean in the region where the planet excess is localized. A horizontal, black, dashed line indicates the best-fit value for K_p . Gray vertical lines are the data, with their uncertainties at 1 standard deviation, while the orange line is the model shown in the middle panel. Black lines are models deviating by less than 2σ from the best fit, while varying the iron abundance, with transparency proportional to their deviation. The bottom half of the panel shows the residuals from the best fit with the same y-axis. A black dashed vertical line shows the best-fit systemic velocity. The average planetary line is in emission, and has a contrast of 84 ppm compared to the continuum.

4.1. Model Grid of the KELT-9b Atmosphere

To compute planetary synthetic spectra, we developed a custom, line-by-line radiative transfer code that implements (1) opacities from the most important optical opacity sources in ultra-hot Jupiters (Fe I, Fe II, Ti I, Ti II, H^- ; Arcangeli et al. 2018; Kitzmann et al. 2018; Lothringer & Barman 2019), and (2) equilibrium chemistry. Local thermal equilibrium (LTE) is assumed throughout the planetary atmosphere, and $\log g_p = 3.3$. We neglected the reflected light component: from a theoretical standpoint, no reflective aerosols are expected in the atmosphere of the planet (Kitzmann et al. 2018); from an observational standpoint, due to the fast rotation of the host star (Gaudi et al. 2017), reflected spectral lines are broadened and thus difficult to detect with our continuum-normalized technique, which removes the majority of their signal. Furthermore, due to the polar orbit of

the planet (Gaudi et al. 2017), the reflected stellar atomic lines would show a variable broadening approximately ranging between the intrinsic broadening of the stellar lines (quadrature) and the rotational broadening of the star (eclipse, 112 km s^{-1}), while the observed broadening is constant and consistent with the expected rotational broadening of the planet ($\sim 6.63 \text{ km s}^{-1}$). We further detail the radiative transfer code in Appendix C. Here we illustrate the parameter space explored.

Our synthetic spectra can be expressed as

$$S\left(\frac{\text{VMR}_{\text{Fe}}}{\text{VMR}_{\text{Fe}^*}}, \frac{\text{VMR}_{\text{Ti}}}{\text{VMR}_{\text{Ti}^*}}, v_{\text{sys}}, K_p, v_{\text{rot,p}}, \text{TP}\right), \quad (2)$$

where $\text{VMR}_{\text{Fe}}/\text{VMR}_{\text{Fe}^*}$ and $\text{VMR}_{\text{Ti}}/\text{VMR}_{\text{Ti}^*}$ are the planetary to stellar iron and titanium volume mixing ratios, $v_{\text{rot,p}}$ is the planetary rotational velocity assumed constant in the atmospheric

region probed by the planetary emission lines, and TP is a suitable parameterization of the temperature pressure profile. At our precision level, we expect retrieved abundances to be degenerate with the rotation rate (due to broadening) and the temperature profile, so that a full exploration of the parameter space is necessary to provide accurate constraints on each parameter. This is beyond the scope of this paper. Instead, we focused on (1) determining which atomic species is mainly responsible for the observed average planetary emission line intersected by the G2 mask and (2) testing the hypothesis that the planet spectrum can be explained assuming abundances consistent with that of its host star. We could thus limit the parameter space by assuming that the planet is tidally locked ($v_{\text{rot,p}} \cdot \sin i_p = 6.63 \text{ km s}^{-1}$). Furthermore, we fixed the thermal profile to the self-consistent temperature profile of KELT-9b that Lothringer et al. (2018) obtained by assuming a planetary metallicity equal to the stellar value and equilibrium chemistry. Under these reasonable assumptions, we produced three groups of models:

$$\begin{aligned} S_{\text{Fe,Ti}} & \left(\frac{\text{VMR}_{\text{Fe}}}{\text{VMR}_{\text{Fe}\star}}, \frac{\text{VMR}_{\text{Ti}}}{\text{VMR}_{\text{Ti}\star}}, v_{\text{sys}}, K_p \right), \\ S_{\text{Fe}} & \left(\frac{\text{VMR}_{\text{Fe}}}{\text{VMR}_{\text{Fe}\star}}, v_{\text{sys}}, K_p \right) \Bigg|_{\text{VMR}_{\text{Ti}}/\text{VMR}_{\text{Ti}\star}=0}, \\ S_{\text{Ti}} & \left(\frac{\text{VMR}_{\text{Ti}}}{\text{VMR}_{\text{Ti}\star}}, v_{\text{sys}}, K_p \right) \Bigg|_{\text{VMR}_{\text{Fe}}/\text{VMR}_{\text{Fe}\star}=0}. \end{aligned} \quad (3)$$

S_{Fe} and S_{Ti} are obtained from $S_{\text{Fe,Ti}}$ by removing titanium and iron, respectively. We fitted v_{sys} and K_p , and simultaneously varied $\text{VMR}_{\text{Fe}}/\text{VMR}_{\text{Fe}\star}$ between 10^{-1} and 10^3 , and $\text{VMR}_{\text{Ti}}/\text{VMR}_{\text{Ti}\star}$ between 3×10^{-3} and 3×10^3 . Since the host star KELT-9 has a metallicity between 0.7 and 2.7 times solar, higher volume mixing ratios seem unlikely. Lower volume mixing ratios would not be detectable at our precision level, and would thus not suffice to explain the data.

4.2. A New Interpretation Scheme for CCFs

The strength of the cross-correlation signal depends on the quality of the match between the binary mask, or the model if used directly, to the data. For example, this can be quantified through peak signal-to-noise ratio. However, this approach is not statistically sound and therefore cannot be used to estimate confidence intervals on planet parameters (Brogi et al. 2016). Alternatives exist, such as the Welch T -test (Brogi et al. 2013) or χ^2 -comparison based on model injection into data (Brogi et al. 2016), but they are computationally expensive. To overcome these challenges, Brogi & Line (2019) presented a cross-correlation to likelihood mapping to perform the comparison in a statistically sound framework (see also Gandhi & Madhusudhan 2019), further generalized by Gibson et al. (2020), while Fisher et al. (2020) proposed a different method based on a random forest approach.

Here, we propose a novel method to directly compare the cross-correlation of models and data. The procedure consists in simulating end-to-end synthetic observations, including the effects of data reduction. In the case of HARPS-N, this is facilitated by the small contamination from telluric lines. Furthermore, HARPS-N is a very stable instrument, built to acquire precise radial velocity observations. Consequently, our

data reduction procedure is relatively simple. We are thus able to simulate end-to-end the effect of the data reduction process on synthetic e2ds HARPS-N generated from our models. This enables a direct comparison using a likelihood function, in a procedure similar to what Kochukhov et al. (2010) have previously suggested to interpret LSD profiles. We cross-checked our new method with the likelihood-mapping by Brogi & Line (2019), finding good agreement (Appendix E).

The first step is simulating the exposure matrix described in Section 2.2:

1. We modeled the star using a PHOENIX model ($T_{\text{eff}} = 10,000 \text{ K}$, $\log g = 4.0$), and applied rotational broadening ($v_{\text{rot,\star}} \cdot \sin i_\star = 111.8 \text{ km s}^{-1}$, Borsa et al. 2019, linear limb darkening coefficient $\epsilon = 0.6$).
2. We convolved each model emission spectrum of the exoplanet with a rotational kernel corresponding to the tidally locked solution ($v_{\text{rot,p}} \cdot \sin i_p = 6.63 \text{ km s}^{-1}$).
3. For each exposure t_i , we Doppler shifted every spectrum for a given orbital solution (K_p, v_{sys}). These velocities were parameters of the fit.

We then processed the simulated time-series through the procedure described in Appendix A. The result was a model exposure matrix for each set of parameters (K_p and v_{sys} ; VMR_{Fe} and VMR_{Ti}), that we could directly fit to observations (see Figure 2). Finally, we computed the Gaussian likelihood for radial velocities between 75 and 252 km s^{-1} , within which the planet trace is expected to be found, by²⁵

$$\log \mathcal{L} = \sum_i [-\log(\sigma_i \sqrt{2\pi}) - \chi_i^2/2], \quad (4)$$

where σ_i and χ_i^2 are the error and χ^2 associated to the data point i . We assumed that σ_i is constant in radial velocity over an exposure, and measured it as the dispersion far from the expected position of the planet (radial velocities between -200 and -100 km s^{-1}). The end result was a multi-dimensional $\log \mathcal{L}$ grid. We then employed different flavors of the likelihood test ratio to assess the significance of each model, to compare the models, and to extract confidence intervals (see Appendix D for practical details on how to do so).

This process is too slow to explore a large four-dimensional grid of parameters. To speed it up, we found that (1) rotational broadening can be included directly in the cross-correlated spectra, and (2) instead of simulating all the exposures for each value of the couple (K_p, v_{sys}), the model exposure matrix can be directly shifted to simulate different values of the couple (K_p, v_{sys}) (see also Brogi & Line 2019). Practically, this assumes that the data reduction process effects on the planetary trace are independent of its K_p and v_{sys} . We tested that neither approximation causes a significant variation of the likelihood distributions.

4.3. Contribution Function of the CCF

Since in our approach we are able to simulate the CCF of each model, for a given assumed atmospheric structure it is possible to directly study the location in pressure where the cross-correlation signal originates. This can be described with a ‘‘contribution function to the CCF at the surface.’’ To our knowledge, this is the first time that the contribution function is

²⁵ The method can be used with any other likelihood function.

adapted to the context of high spectral resolution observations of planetary atmospheres. We define it here by analogy with the classic contribution function to the flux at the surface.

Following, e.g., Irwin (2009) and Malik et al. (2019) we define the contribution functions as the contribution of each discrete layer in our model to the flux at the surface of the planetary atmosphere. In our case, we locate the “surface” high up in the optically thin region of the planet atmosphere, from which the photons escape and reach the observer. If every layer n emits an intensity $\Delta_n I(\mu)$ in a direction $\mu = \cos \theta$, we can write

$$I(\mu) = \sum_n [\Delta_n I(\mu) \exp(-\tau_n/\mu)], \quad (5)$$

where τ_n represents the optical depth above layer n , and $\Delta_n I$ is computed according to the linear in optical depth approximation (Toon et al. 1989). The n th term in square brackets on the right-hand side of the equation is the contribution function of layer n .

We now apply the cross-correlation at the left-hand and right-hand side of Equation (5). The sum over n atmospheric layers can be commuted with the sums contained in our definition of CCF (Equation (B2)). As a result, we can write

$$\begin{aligned} \text{CCF}(I(\mu)) &= \text{CCF}\left(\sum_n [\Delta_n I(\mu) \exp(-\tau_n/\mu)]\right) \\ &= \sum_n \text{CCF}([\Delta_n I(\mu) \exp(-\tau_n/\mu)]). \end{aligned} \quad (6)$$

By extension, the n terms in square brackets in the right-hand side of Equation (6) represent the “contribution functions of the CCF” of each layer. Physically, they represent the contribution to the intensity as a function of radial velocity rather than wavelength from every atmospheric layer.

With this definition, it is trivial to identify the pressure range that can be probed with a line-weighted binary mask CCF of high spectral resolution observations. Furthermore, for a given model, the contribution functions of the CCF tell us which pressure layers more tightly constrain the radial velocity of the planet. By integrating over μ one obtains expressions for the flux.

5. Results from Model Comparison

In the following, we provide our interpretation of the average planet line intersected by the G2 mask based on model comparison.

5.1. Fit with Line-weighted Binary Mask

We first identified which among the models defined in Equation (3) best explains the data. The model containing only lines from neutral and ionized titanium and no atmospheric iron, S_{Ti} , has maximum likelihood at the highest allowed abundances of titanium. This suggests that titanium lines are too weak to explain the observed emission lines even when $\text{VMR}_{\text{Ti}} = 3000 \cdot \text{VMR}_{\text{Ti},\star}$. We then compared S_{Ti} to the full model $S_{\text{Fe,Ti}}$ with a likelihood test ratio (see Appendix D), and found that it can be excluded at 4.3σ . When limiting the maximum abundance of titanium to 100 times the stellar value, the model can be excluded at 5.1σ . As a further indication that iron is necessary to explain the observed emission line, we calculated the difference in Bayesian Information Criterion

Table 1
Comparison of Models Containing Iron or Titanium Lines

	ΔBIC with $S_{\text{Fe,Ti}}$	LRT with $S_{\text{Fe,Ti}}$
S_{Fe}	-8.7	$<0.1\sigma$
S_{Ti}	+10	4.3σ

Note. The likelihood ratio test metric indicates that a model containing neutral and ionized iron (S_{Fe}) explains the data as well as a model containing also neutral and ionized titanium. On the other hand, a model containing only lines from neutral and ionized titanium (S_{Ti}) does significantly worse. Furthermore, the Bayesian Information Criterion difference favors the model containing only neutral and ionized iron, and no titanium, due to the smaller number of free parameters. We thus adopt S_{Fe} as the fiducial model.

(BIC; Liddle 2007) and found that $\min[\text{BIC}(S_{\text{Ti}})] = \min[\text{BIC}(S_{\text{Fe,Ti}})] + 10$. The difference increases to 17.5 when limiting the maximum abundance of titanium to 100 times the stellar value, indicating strong preference for the presence of iron.

In a similar fashion, we compared the model containing only lines from neutral and ionized iron and no atmospheric titanium, S_{Fe} , to the full model. In this case, the null hypothesis that S_{Fe} is the true model cannot be excluded ($<0.1\sigma$). Furthermore, it is strongly favored by the BIC test, with $\min[\text{BIC}(S_{\text{Fe}})] = \min[\text{BIC}(S_{\text{Fe,Ti}})] - 8.7$, which penalizes the presence of an additional parameter in $S_{\text{Fe,Ti}}$. We thus adopted S_{Fe} as our nominal model to derive planetary parameters (see Table 1).

The best-fit parameters are $K_p = 242 \text{ km s}^{-1}$, $v_{\text{sys}} = -22.5 \text{ km s}^{-1}$, $\text{VMR}_{\text{Fe}} = 30 \cdot \text{VMR}_{\text{Fe},\star}$. The model is a very good match to the data, as evidenced by a reduced $\chi^2 = 6128/5874 = 1.043$ and by residuals within the statistical fluctuations (Figure 2). We computed the significance of the model by performing a likelihood test ratio (LRT), comparing it to the case of null detection $\text{VMR}_{\text{Fe}} = 0$ (a straight line; see Appendix D). The detection is significant at 6.15σ . As a further test, we computed that the BIC value of our best-fit model is lower by 24.5 compared to the null detection, indicating a strong preference for the presence of iron. The 1σ confidence intervals for the three parameters (see Appendix D) are $238 \text{ km s}^{-1} < K_p < 247.5 \text{ km s}^{-1}$, $-32 < v_{\text{sys}} < -19$, and $10 < \text{VMR}_{\text{Fe}}/\text{VMR}_{\text{Fe},\star} < 150$ (compatible with a few times the stellar value at 2σ).

Finally, we compared our nominal model S_{Fe} with two models where we suppressed lines by neutral and ionized iron respectively. These two models are not formally nested in S_{Fe} , and we compared instead the significance yielded by the best-fit parameters for each model. When only neutral iron is present, the results are nearly indistinguishable from the full model S_{Fe} , with a similar significance, best fit, and confidence interval. On the other hand, when only ionized iron is present, the best fit is found at the upper limit of $\text{VMR}_{\text{Fe}} = 1000 \cdot \text{VMR}_{\text{Fe},\star}$, and has a much lower significance of 3.1σ . In this case, the BIC test favors the null detection, indicating that the ionized iron lines intersected by the G2 mask are too weak to explain the observed planetary feature alone (see Table 2).

We also applied the method by Brogi & Line (2019) to perform an independent test (see Appendix E). In this case, we fixed the abundance to its best-fit value, and retrieved K_p and v_{sys} and a scale factor which is a proxy for abundance. The

Table 2

Comparison of Models Containing Neutral Iron Lines, Ionized Iron Lines, or Both

	ΔBIC with Null Detection	LRT with Null Detection
Neutral and ionized iron (S_{Fe})	-25	6.15 σ
Neutral iron only	-25	6.15 σ
Ionized iron only	+5	3.1 σ

Note. The likelihood ratio test metric indicates that a model containing only ionized iron has a lower significance compared to the null detection. Although the significance is still at the 3σ level, this occurs at the upper limit of the allowed iron abundances (1000 times solar), and the Bayesian Information Criterion test significantly disfavors this model compared to a flat line. Neutral iron is thus necessary to explain the data under our assumptions. Furthermore, The addition of ionized iron does not significantly improve the fit, or significantly change the inferred iron abundance.

results are in good agreement with those found with our novel framework (see Figure 3, and Appendix E).

5.2. Reference Frame of the Signal

The comparison at face-value of the joint probability distributions and the marginalized 1D probabilities reveals that our results are consistent with all literature values of the systemic velocity (Gaudi et al. 2017, adopted by Yan & Henning 2018; Hoeijmakers et al. 2019; Borsa et al. 2019; see Table 3). While these authors reported individual precisions around 0.1 km s^{-1} , the measured values are significantly discrepant, spanning a range of about 3 km s^{-1} . Further analysis is required to pinpoint the origin of this discrepancy. We thus attributed an error of 3 km s^{-1} to the single measurements to account for an unknown systematic effect. With this assumption, the average $v_{\text{sys},*} = -19 \pm 3 \text{ km s}^{-1}$ is compatible within 1σ with our result ($\Delta v_{\text{sys},*} = 3.5_{-4.5}^{+5.5} \text{ km s}^{-1}$ and $\Delta v_{\text{sys},*} = 1_{-4}^{+3} \text{ km s}^{-1}$ for the line-weighted binary mask and the Brogi & Line 2019 approaches respectively).

Furthermore, deviations between K_p measured from atomic metal lines in emission (our work) and in transmission (Hoeijmakers et al. 2019) are in agreement at the 2σ level. However, the K_p value measured by Yan & Henning (2018) on the $\text{H}\alpha$ line is in tension with K_p measured on the metal lines ($\Delta K_p = 27_{-8}^{+7.5} \text{ km s}^{-1}$ and $\Delta K_p = 27.5 \pm 6 \text{ km s}^{-1}$ for the line-weighted binary mask and Brogi & Line 2019 approaches respectively). We explored the possibility that this difference is of astrophysical origin, due to the fact that the hydrogen and iron lines probe different regions of the atmosphere. Yan & Henning (2018) report that the $\text{H}\alpha$ line approaches but does not reach the Roche lobe. Furthermore, the $\text{H}\alpha$ line has a symmetrical profile. Therefore, it is likely generated below the exosphere, in the part of the atmosphere gravitationally bound to KELT-9b. Any relative motion between the gas components probed by observations should thus be subsonic. By assuming the adiabatic coefficient of a monoatomic gas, the temperature profile by Lothringer et al. (2018) and the mean molecular weight from our model, we obtain that the sound speed ranges between 6.5 and 8.5 km s^{-1} . If it were of astrophysical origin, the difference between the semi-amplitude measured by Yan & Henning (2018) and our measurement would thus be larger than the sound speed (although only

marginally in the case of the line-weighted binary mask), which is unlikely. Further dedicated work is necessary to consistently explain these observations.

6. Discussion

6.1. A Temperature Inversion in the Dayside of KELT-9b

The average planet line intersected by the G2 mask is in emission, which can only be explained if a thermal inversion is present in the atmosphere of KELT-9b. This conclusion is model-independent, since it only hinges on the sign of the planetary lines, which is preserved by our analysis.

We calculated the contribution functions to the CCF of the model adopting the thermal inversion by Lothringer et al. (2018) and solar iron abundance (Section 4.3). The emission from the neutral iron line cores originates between 10^{-3} and 10^{-5} bar (see Figure 4). This is higher up compared to the ~ 30 mbar region probed by Hooton et al. (2018), who reported evidence of inversion using ground-based photometry. It is also well within the inverted region of the atmosphere, found above the region of absorption of stellar irradiation and located between 1 and 100 mbar in the optical region probed by HARPS-N (Lothringer et al. 2018).

For hot Jupiters with equilibrium temperature larger than 1600 K, molecules with strong optical opacities such as TiO and VO are expected to be in the gas phase, causing a temperature inversion below 0.1 bar (Hubeny et al. 2003; Fortney et al. 2008). For the higher temperatures experienced by ultra-hot Jupiters, most molecules are dissociated, so these species become irrelevant for the thermal inversion. Instead, atomic metals and metal hydrides are capable of absorbing enough short-wavelength irradiation to heat up the atmosphere. In particular, the bound-bound transitions of neutral iron absorb significantly longward of $0.3 \mu\text{m}$, and the bound-free transitions absorb the high-energy flux shortward of $0.3 \mu\text{m}$ (Sharp & Burrows 2007). This is enough to create a thermal inversion at 10 mbar (Lothringer et al. 2018). Higher up, around 0.5 mbar, iron is mostly found in its ionized form due to the high atmospheric temperature.

A second important factor that contributes to the formation of thermal inversions is the lack of molecules with near-infrared opacities, able to radiatively cool the atmosphere. This can be caused by high C/O atmospheres (Mollière et al. 2015; Gandhi & Madhusudhan 2019) and/or by thermal dissociation (Arcangeli et al. 2018; Lothringer et al. 2018; Parmentier et al. 2018), with the latter scenario predicted to be important in ultra-hot Jupiters (Lothringer & Barman 2019; Malik et al. 2019).

6.2. On the Chemical Composition of KELT-9b

Ultimately, we conclude that the average KELT-9b emission line intersected by the G2 mask can be explained with neutral iron as predicted by equilibrium chemistry, with iron abundance compatible with a few times that of the host star. However, our results do not imply a lack of ionized iron lines or other species. Furthermore, with the current analysis, our confidence intervals on VMR_{Fe} are likely too narrow. This is because (1) we fixed the thermal profile and rotation rate and (2) the choice of a specific mask inherently biases the results by selecting specific pixels within the spectrum.

Looking forward, an application of our method with additional line-weighted masks sensitive to different lines,

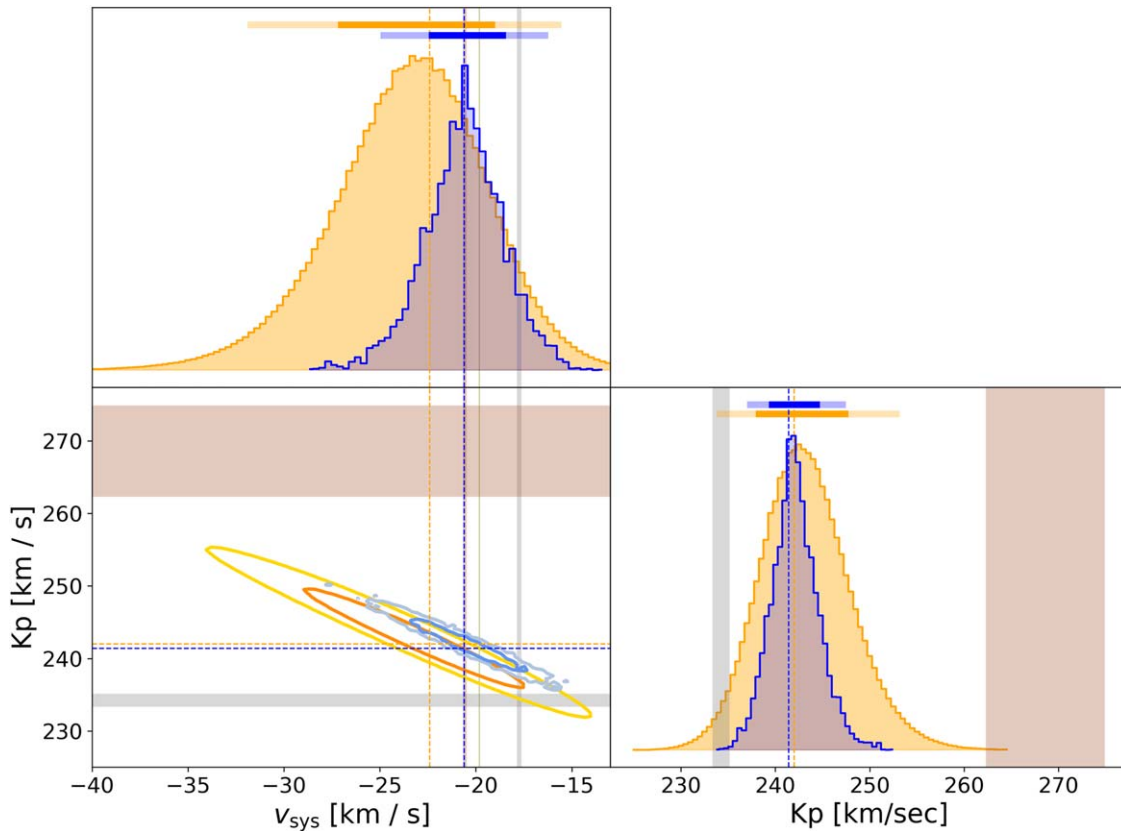


Figure 3. Marginalized likelihood distributions for v_{sys} and K_p for the line-weighted binary mask (orange) and for the Brogi & Line (2019) approach (blue). Dark and light orange (blue) horizontal bars denote the 1σ and 2σ confidence levels. Orange (blue) dashed lines indicate the best-fit value. Shaded areas denote the literature values by Yan & Henning (2018) (sienna), Hoeijmakers et al. (2019) (gray) and (Borsa et al. 2019) (olive). Borsa et al. (2019) only measure v_{sys} . Our distribution for v_{sys} is consistent with the literature, while we deviate from the K_p value by Yan & Henning (2018) by about 3σ .

Table 3
Literature and Derived v_{sys} and K_p Values

	v_{sys} (km s $^{-1}$)	K_p (km s $^{-1}$)
Yan & Henning (2018)	-20.6 ± 0.1^a	$269_{-6}^{+6.5}$
Borsa et al. (2019)	-19.81 ± 0.02	...
Hoeijmakers et al. (2019)	-17.7 ± 0.1	234.24 ± 0.9
This work, G2 mask	$-22.5_{-4.5}^{+3.5}$	242_{-4}^{+5}
This work,	$-20.5_{-1.5}^{+2}$	241.5_{-2}^{+3}
Brogi & Line (2019) technique		

Notes. The error bars indicate 1σ intervals reported in the literature, or on the 1D marginalized likelihoods. Our results are broadly consistent with the literature, with the exception of K_p measured by Yan & Henning (2018). When both are measured from the planetary spectrum, systemic velocity and Keplerian velocity are correlated, as evident from Figure 3, where the 2D confidence intervals are reported.

^a Taken from Gaudi et al. (2017).

and with additional models exploring different thermal profiles, may provide an avenue to measure an [Fe/H] potentially representative of the whole planetary atmosphere. Indeed, iron condenses through a simple phase transition, passing to the liquid or solid state. When present, iron clouds effectively remove most of the iron from the atmosphere above them (Visscher et al. 2010). The mere presence of iron lines in the atmosphere of a planet indicates the likely absence of deep iron clouds, suggesting that the measured abundance may be

representative of the global iron abundance in the planetary atmosphere.

6.3. Comparison of Transmission and Emission Spectroscopy of Iron Lines

The transmission spectrum of the planet atmosphere probes its terminator region, where lower temperatures are expected, which could be reflected in different chemical properties of the atmosphere. Hoeijmakers et al. (2019) reported absorption from neutral iron at the terminator of KELT-9b at the millibar level by assuming the pressure level of the planetary continuum. This would be at a similar pressure to what we report here looking at the dayside emission line. Hoeijmakers et al. (2019) also reported the detection of ionized iron lines, which they estimated to be at the μbar level, higher up compared to the pressure level where neutral iron emission lines originate in our scenario. The combination of these results covers three orders of magnitude in pressure, although we highlight that we find no evidence for ionized iron with our analysis.

From a geometrical standpoint, transmission spectroscopy is sensitive to lower densities compared to emission spectroscopy. Therefore, the combination of the transmission and emission findings could suggest that neutral iron is depleted at around 0.1 mbar at the terminator compared to the dayside atmosphere of the planet. However, we emphasize that, for both the emission and transmission studies, the pressure levels where spectral features originate were calculated by making

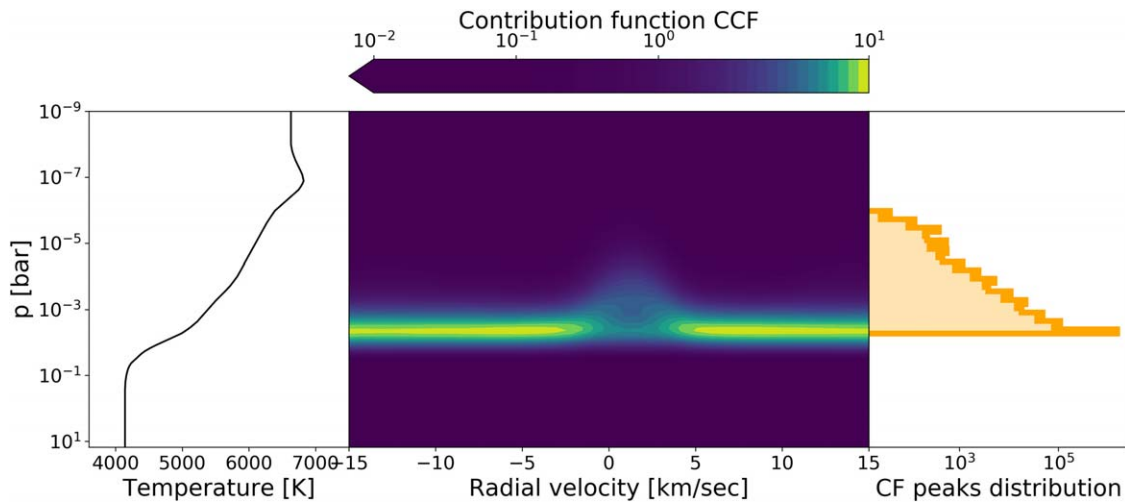


Figure 4. Diagnostics of the contribution functions of a model assuming stellar iron abundance and the temperature–pressure profile by Lothringer et al. (2018) (shown in the left panel). Central panel: cross-correlation of the contribution function, performed layer by layer. This indicates the relative contribution to the flux as a function of radial velocity rather than wavelength (see Section 4.3). The continuum of the cross-correlation function (CCF) is located around a few bars, and is due to absorption by H^- . The peak of the CCF is mostly sensitive to pressure levels around $10^{-3/-5}$ bar. Right panel: for every wavelength channel in our model, we look for the location in pressure of the maximum of the contribution function, and produce a histogram. The two separated peaks show that the continuum originates at the pressure of a few bars, and that the cores of most of the iron lines originate between pressures of $10^{-3/-5}$ bar (note the logarithmic scale of the counts).

assumptions regarding the temperature profile and gravity of the planet, and assuming a hydrostatic profile for the atmosphere. Further work to explore the effect of these assumptions is required to properly combine the data sets. Nevertheless, this comparison demonstrates the potential to characterize the 3D structure of the atmosphere of exoplanets by studying them at high spectral resolution both in transmission and emission.

L.P. acknowledges helpful discussions with the exoplanet atmosphere team at Anton Pannekoek institute for astronomy, particularly K. Todorov and J. Arcangeli, and with Phil Uttley. We thank the anonymous referee, whose insightful feedback improved the quality and clarity of the manuscript. L.P. thanks P. Mollière for the prompt support with the validation of the radiative transfer code. The research leading to these results has received funding from the European Research Council (ERC) under the European Union’s Horizon 2020 research and innovation programme (grant agreement No. 679633 and No. 724427; Exo-Atmos and FOUR ACES). Based on observations made with the Italian Telescopio Nazionale Galileo (TNG) operated on the island of La Palma by the Fundación Galileo Galilei of the INAF at the Observatorio Roque de los Muchachos. This work has made use of the VALD database, operated at Uppsala University, the Institute of Astronomy RAS in Moscow, and the University of Vienna. This research made use of Astropy,²⁶ a community-developed core Python package for Astronomy (Astropy Collaboration et al. 2013, 2018). J.M.D. acknowledges support by the Amsterdam Academic Alliance (AAA) Program. M.B. acknowledges support from the UK Science and Technology Facilities Council (STFC) research grant ST/S000631/1. L.M. acknowledges support from the University of Rome Tor Vergata through “Mission: Sustainability 2017” fund. G.S. acknowledges financial support from “Accordo ASI/INAF” No. 2013-016-R.0 2013 July 9 and 2015 July 9. R.A. acknowledges the financial support of the SNSF. We acknowledge support from

the INAF/Frontiera project through the “Progetti Premiali” funding scheme of the Italian Ministry of Education, University, and Research.

Appendix A

A Physical Interpretation of the CCF

In this Appendix we aim to provide a physical understanding of the planetary excess observed in Figure 2. This step is fundamental to properly set-up the simulations to be compared with data. We thus describe in mathematical detail (1) how the observations are related to the planetary and stellar spectrum and (2) the steps undertaken to normalize the spectral observations described in Section 2.1. The steps involved:

1. a color-correction, to mitigate chromatic losses that change the spectral shape observed over the night; this was particularly important for our observations, due to the failure of the atmospheric dispersion corrector (ADC) which corrects part of these effects at the telescope level;
2. a rescaling of the spectrum to its continuum in every order, to account for variations of the signal-to-noise overnight;
3. a normalization to the stellar spectrum, obtained directly from the data, to remove stellar lines.

A.1. Relation between Observations and Planetary and Stellar Spectra

HARPS-N records combined-light observations of the star and planet system at any given time in units of photoelectron counts $C(\lambda_n, t_i)$, split in orders m (e2ds spectra). In other words, the information they contain is the total energy deposited in each pixel n during the exposure i . On the other hand, both the PHOENIX models and our radiative transfer code output a spectral flux density, i.e., energy per unit wavelength per unit area per unit time $F(\lambda_n, t_i)$. We assume that these quantities are

²⁶ <http://www.astropy.org>

related by

$$C(\lambda_n, t_i) = \text{LSF} * \{ [R_p^2 \cdot F_p(\lambda_n, t_i) + R_*^2 \cdot F_*(\lambda_n)] \cdot \mathcal{A}(\lambda_n, t_i) \cdot \mathcal{B}(t_i) \} \times (\lambda_n, t_i) \cdot \Delta t_i \cdot \frac{A_{\text{tel}}}{d^2} \cdot \Delta \lambda_n \cdot \mathcal{G}, \quad (\text{A1})$$

where Δt_i is the exposure time, A_{tel}/d^2 is the ratio of the area of the telescope to the distance of the system squared, $\Delta \lambda_n$ is the wavelength range covered by the pixel n , and \mathcal{G} is a gain factor. We added two factors \mathcal{A} and \mathcal{B} to indicate chromatic losses (\mathcal{A} ; e.g., chromatic losses at the fiber entrance due to atmospheric dispersion) and overall flux losses (\mathcal{B} ; e.g., seeing variations, airmass effects). While \mathcal{B} is a simple scaling factor between the exposures, \mathcal{A} changes the shape of the spectrum in each exposure.

The relation is nonlinear because the line-spread function of the spectrograph is convolved with the received spectral flux density, and the planet and star fluxes are already convolved with the respective rotational broadening kernel. In the rest of the discussion we assume that $C(\lambda_n, t_i)$ is proportional to $F(\lambda_n, t_i) = R_p^2 \cdot F_p(\lambda_n, t_i) + R_*^2 \cdot F_*(\lambda_n)$, which we find true at a precision better than 0.1 ppm (see also Pino et al. 2018b).

After having related observations and models, we turn to understanding how the data reduction process that we follow impacts the models in mathematical detail. With this next passage, we get a physical understanding of what the observed CCF (Figure 2) means.

A.2. Preparation of Spectra for Cross-correlation

To combine the spectra in order to increase the signal-to-noise ratio, and properly extract the planet signal, the data reduction process aims at removing the time and wavelength dependence of $\mathcal{A}(\lambda_n, t_i)$ and $\mathcal{B}(t_i)$.

The first step is color-correction, which removes the wavelength dependence of these multiplicative noise factors. Color-correction is performed relative to a template, for which we used the first spectrum of the night, where the ADC was performing the best. We produced a low-resolution version of each spectrum, with a single point in every order. To remove temporal variations, every low-resolution spectrum is rescaled to its spectral order 48 ($5580 \text{ \AA} < \lambda < 5640 \text{ \AA}$):

$$C_{\text{LR}}(\lambda_n, t_i) = \frac{\langle C(\lambda_n, t_i) \rangle_{\text{order } m}}{\langle C(\lambda_n, t_i) \rangle_{\text{order } 48}} = \frac{\langle F(\lambda_n, t_i) \mathcal{A}(\lambda_n, t_i) \rangle_{\text{order } m}}{\langle F(\lambda_n, t_i) \mathcal{A}(\lambda_n, t_i) \rangle_{\text{order } 48}} \quad (\text{A2})$$

where we used Equation (A1), angular brackets indicate average between pixels 1024 and 3072 of each order, and we simplified several wavelength-independent factors. By assuming that the factor $\mathcal{A}(\lambda_n, t_i)$ is approximately a constant $\mathcal{A}(t_i)_m$ over an order m and that the planet flux is small compared to the star, we obtain a residual curve for each exposure i :

$$\frac{C_{\text{LR}}(\lambda_n, t_i)}{C_{\text{LR,templ}}(\lambda_n)} = \frac{\mathcal{A}(t_i)_m}{\mathcal{A}_{\text{templ},m}}. \quad (\text{A3})$$

Equation (A3) represents the variation of each spectrum compared to a template only due to the color effect, and needs to be removed from the spectra. We determined that an

interpolation with a sixth-order spline in wavelength at each λ_n for each exposure minimizes the residuals. We then obtain a color-corrected version of C by dividing Equation (A1) by Equation (A3):

$$C_{\text{cc}}(\lambda_n, t_i) = \text{LSF} * \{ F(\lambda_n, t_i) \cdot \mathcal{A}_{\text{templ}}(\lambda_n) \cdot \mathcal{B}(t_i) \} \cdot \Delta t_i \cdot \frac{A_{\text{tel}}}{d^2} \cdot \Delta \lambda_n \cdot \mathcal{G}. \quad (\text{A4})$$

Some extra time-dependent (and wavelength-independent) factors have been absorbed in $\mathcal{B}(t_i)$. We stress that color correction only ensures that the relative shape of spectra is the same and is not enough to perform spectrophotometry. Indeed, any deviation from the real shape of the spectrum is carried over to the other exposures through the factor $\mathcal{A}_{\text{templ}}(\lambda_n)$.

Now that the shape of the spectra is adjusted, it is possible to remove the overall flux level fluctuations $\mathcal{B}(t_i)$. This is done by rescaling each spectrum order by order to its average:

$$[C_{\text{cc,r}}(\lambda_n, t_i)]_m = \frac{[C_{\text{cc}}(\lambda_n, t_i)]_m}{\langle C_{\text{cc}}(\lambda_n, t_i) \rangle_m} = \frac{[F(\lambda_n, t_i)]_m}{\langle F(\lambda_n, t_i) \rangle_m}, \quad (\text{A5})$$

where we have used the independence of $\mathcal{B}(t_i)$ from wavelength, and assumed that $\mathcal{A}_{\text{templ}}(\lambda_n)$ can be brought out of the average within order m . At this point, the spectra have the same level in the continuum and can be combined.

Now, recall that $F \propto R_p^2 \cdot F_p(\lambda_n, t_i) + R_*^2 \cdot F_*(\lambda_n)$. While the star is assumed to be stable over the course of an observation, the planetary spectral lines move as a result of its Doppler motion, hence its time dependence. Our aim is now to remove $R_*^2 \cdot F_*$ to isolate the planet signal. This is done by building a master spectrum M_* containing only the stellar spectrum and the planetary continuum, and normalizing each exposure by the master spectrum. As is common in the literature, we obtain the master spectrum with a median in time of the color-corrected, rescaled spectra, Equation (A5). Since the planet moves in time by about 0.5–3.5 pixels per exposure, its lines are mostly removed from the master. By splitting the planet flux in its line and continuum contribution ($F_{\text{p,lines}}$ and $F_{\text{p,cont}}$)

$$[M]_m = \text{med}_t [C_{\text{cc,r}}(\lambda_n, t_i)]_m \approx \frac{[F_*(\lambda_n) + F_{\text{p,cont}}(\lambda_n)]_m}{\langle F_*(\lambda_n) + F_{\text{p,cont}}(\lambda_n) \rangle_m}, \quad (\text{A6})$$

where we neglected the flux contained in the planetary spectral lines at the denominator. Finally, by dividing $C_{\text{cc,r}}(\lambda_n, t_i)$ by the master spectrum, we obtain

$$[C_{\text{cc,r,tn}}(\lambda_n, t_i)]_m = \frac{[C_{\text{cc,r}}(\lambda_n, t_i)]_m}{[M(\lambda_n)]_m} = \frac{R_p^2 \cdot [F_{\text{lines p}}(\lambda_n, t_i)]_m}{[R_*^2 \cdot F_*(\lambda_n) + R_p^2 \cdot F_{\text{p,cont}}(\lambda_n)]_m} + 1. \quad (\text{A7})$$

What we measure is thus the planetary lines normalized to the stellar plus planetary continuum.

Finally, we applied a high-pass filter by computing the standard deviation of each pixel in time (i.e., across the full spectral sequence) and applying a threshold three times above the median level of the noise (the exact choice for the threshold level does not influence the final result). For each exposure and each order, we fitted a second-order polynomial to the spectra

after rejecting strong outliers and masked pixels. We then divided the data by the fitted polynomial. Eventually, we applied the CCF.

The planet continuum itself cannot be recovered. Indeed, the rescaling in Equation (A5) must be carried out order by order, because within one order $\mathcal{A}(\lambda_n, t_i)$ is approximately constant. The same holds for the planetary continuum, which is thus removed from our analysis as a by-product. Alternative approaches use a polynomial normalization, with the same outcome. Recently, Cauley et al. (2019) claimed that they performed flux calibration on Echelle spectra similar to ours. Such an approach has a potentially enormous impact on the study of exoplanet atmospheres with this technique, because it would preserve the planetary continuum, which would already be detectable with currently achieved precisions (Pino et al. 2018b).

Appendix B Line-weighted, Binary Mask CCF

Functionally, this CCF is a weighted average of a wavelength-dependent signal $S(\lambda)$, in our case the planetary spectrum normalized to the continuum (Appendix A.2), on the spectral lines considered in the mask,

$$\text{CCF}(v) = \frac{\sum_{\text{orders}} w_{\text{order}} \sum_{i=1}^{N_{\text{lines}}} \int_{\text{order}} S(\lambda) \cdot M_i(\lambda)|_v \cdot w_i d\lambda}{\sum_{\text{orders}} w_{\text{order}} \sum_{i=1}^{N_{\text{lines}}} \int_{\text{order}} M_i(\lambda)|_v w_i}. \quad (\text{B1})$$

Within each order, to each of the N lines considered, we associate a binary mask M_i that has a value of 1 within a wave band 0.82 km s^{-1} wide (1 HARPS-N nominal pixel) around each considered line shifted to account for a radial velocity v , 0 elsewhere. Each order is weighted according to the signal-to-noise ratio of the observations ($w_{\text{order}} = 1/\sigma_{\text{order}}$, where σ_{order} is the photometric dispersion of the order computed between pixels 1024 and 3072, and only orders with signal-to-noise ratio larger than 35 are kept), and each line is weighted (w_i) according to its information content. In the case of the G2 mask that we used, this is the contrast of the spectral line, but different applications may require different weighting schemes. Since the width of the masks in the wavelength space changes with radial velocity, it is important to compute the normalization at every value of v .

Computationally, it is convenient to recast Equation (B1) to have an effective weight for every pixel in the detector. Practically, each binary mask can span one or more complete pixels and fractions of pixels at the edges. For a single line i , we can expand the integral by co-adding contributions from each pixel or pixel part that falls within the binary mask M_i . If we label each pixel by j , and call $\Delta\lambda_j$ the width of the pixel in wavelength space, then pixels entirely within the mask contribute to the spectrum with $\overline{\Delta\lambda_j} = \Delta\lambda_j$, while pixels at the edges of the mask contribute with $\overline{\Delta\lambda_j} < \Delta\lambda_j$. Thus:

$$\text{CCF}(v) = \frac{\sum_{\text{orders}} \sum_{i=1}^{N_{\text{lines}}} \sum_{j=1}^{N_{\text{pixels in } M_i|_v}} S(\lambda_j) \cdot (w_{\text{order}} \cdot w_i \cdot \overline{\Delta\lambda_j})}{\sum_{\text{orders}} \sum_{i=1}^N \sum_{j=1}^{N_{\text{pixels in } M_i|_v}} (w_{\text{order}} \cdot w_i \cdot \overline{\Delta\lambda_j})}. \quad (\text{B2})$$

The term in parenthesis is the effective weight for each pixel in each order, and is a unique property of each mask considered.

Written in this form, the calculation can be conveniently performed using matrix calculation.

We computed the CCF in each order of each exposure by sliding the binary mask between -400 and 400 km s^{-1} in steps of 2.7 km s^{-1} (one nominal HARPS-N resolution element, containing about three nominal HARPS-N pixels). With this choice, we were entitled to treat each CCF point as statistically independent from the others, since their information comes from separate resolution elements. For each exposure, we then obtained a total CCF by summing the CCFs of each single order. With a similar procedure, we computed the normalization at the denominator in Equation (B2).

The peak of the CCF is found at a different position in every exposure, due to the planet motion around its host. The juxtaposition of all exposures provides a planet trace. We then assumed a circular orbit for the planet and shifted the CCF in each exposure for different values of the tangential velocity of the planet K_p . For every combination, we interpolated the total CCFs in each exposure to a common velocity grid, and summed them. The resulting 1D CCF is maximized when the individual exposures are correctly aligned in the rest-frame of the planet.

Appendix C Radiative Transfer Code

We solved the radiative transfer equation in its integral form, employing a ‘‘linear in optical depth’’ approximation for the source function, which is valid for a non-scattering atmosphere (Toon et al. 1989). We employed 200 logarithmically spaced layers between 10^5 and 10^{-12} bar, covering the full region where lines are generated with enough spatial resolution. This was verified with a step doubling procedure.

For a given temperature–pressure profile, we assumed equilibrium chemistry and calculated volume mixing ratios using the publicly available `FastChem` code version 2 (Stock et al. 2018; J. W. Stock et al. 2020, in preparation). Our opacities are calculated by employing the VALD3 database (Baschek et al. 1970; Bridges 1973; Blackwell et al. 1980; Kroll & Kock 1987; Fuhr et al. 1988; Martin et al. 1988; Pauls et al. 1990; Bard et al. 1991; O’Brian et al. 1991; Hannaford et al. 1992; Bizzarri et al. 1993; Bard & Kock 1994; Ryabchikova et al. 1994, 1997, 1999, 2015; Piskunov et al. 1995; Nitz et al. 1998; Raassen & Uylings 1998; Kupka et al. 1999, 2000; Barklem et al. 2000; Pickering et al. 2001; Barklem & Aspelund-Johansson 2005; Blackwell-Whitehead et al. 2006; Kurucz 2010, 2013, 2014; Lawler et al. 2013; Wood et al. 2013). While the VALD3 database offers line lists for a variety of atomic and molecular species, we limited this study to Fe I, Fe II, Ti I, Ti II, expected to be the most spectrally active species in KELT-9b (Hoeijmakers et al. 2018). We computed opacity tables by broadening the lines with a Voigt profile accounting for thermal and natural broadening, and we used partition functions by Barklem & Collet (2016) to obtain opacities as a function of temperature, over a fine grid in wavelength ($\Delta\lambda = 0.001 \text{ \AA}$) over the full HARPS-N range. At this resolution, the single lines in the atmosphere are resolved by a factor of 20–30, making our code effectively line-by-line. Our H^- bound-free opacity comes from John (1988), in particular their Equation (4). We also note a possible imprecision in the units for λ_0 and $\alpha = hc/k_b$ in that paper, which appear to be inconsistent. If λ_0 is taken in μm as the author suggests, the correct value for α to insert in Equation (3)

is 1.439×10^4 rather than 1.439×10^8 . We validated our code by reproducing the position and depth of iron lines in a $\log g = 4.5$, $T_{\text{eff}} = 4500$ K PHOENIX model (Husser et al. 2013), adopting the temperature profile provided in the “ATMOS.fits” file. For such a star, iron lines are modeled in LTE, which we also assumed. We did not attempt to reproduce the pressure broadened wings and microturbulence broadening in the stellar spectrum, because HARPS-N is only sensitive to the core of the planetary iron lines and microturbulence is degenerate with rotational broadening at our level of precision. We also validated the continuum in our model by reproducing it with petitRADTRANS (Mollière et al. 2019), finding agreement to within a few percent over the HARPS-N range.

Appendix D

Significance of the Detection, Model Comparison, and Confidence Intervals

This Appendix presents practical details on how we treated $\log \mathcal{L}$ to (1) assess the significance of our detection, (2) perform model comparison, and (3) extract confidence intervals. All of these tasks can be performed using Wilks’ theorem (Wilks 1938). An extensive literature on the topic is available (e.g., Lampton et al. 1976 treat most of these problems in a very clear manner), and we specialize the discussion to our method. We also provide a practical method to marginalize the likelihood distribution.

Given a model S with p parameters, a model S_{nested} is nested to it if it can be obtained from S by fixing $q < p$ parameters. In this case, $\max \mathcal{L}(S) \geq \max \mathcal{L}(S_{\text{nested}})$. Wilks’ theorem states that the LRT metric

$$\begin{aligned} \text{LRT} &= -2 \ln \frac{\max \mathcal{L}(S_{\text{nested}})}{\max \mathcal{L}(S)} \\ &= -2 \ln [\max \mathcal{L}(S_{\text{nested}}) - \max \mathcal{L}(S)] \end{aligned} \quad (\text{D1})$$

is distributed as a χ^2 distribution with q degrees of freedom under the null hypothesis that S_{nested} is true.

The application to model comparison is straightforward: in our case, S_{Fe} and S_{Ti} are nested in $S_{\text{Fe,Ti}}$, and $q = 1$. The survival function of a χ^2 distribution with one degree of freedom evaluated in LRT gives the probability that the measured LRT difference would be observed by chance alone. A high probability indicates that the null hypothesis that the nested model is true can be excluded. We convert this probability to σ values using a two-tailed Gaussian distribution.

To assess the significance of the detection, we created a nested model with $\text{VMR}_{\text{Fe}} = 0$. We then compared this to our preferred model S_{Fe} . Using the properties of (D1), we computed the probability at which the hypothesis that no spectral line is present can be excluded (again, $q = 1$).

It is maybe less evident that the same theorem allows us to compute confidence intervals. A clear explanation is found in Cash (1976), which we summarize. Assume that we are interested in the confidence interval on parameter θ , which can have values $(\bar{\theta}_1, \bar{\theta}_2, \dots)$. First, we fix $\theta = \bar{\theta}_1$, and look for the maximum likelihood by varying the rest of the parameters. Practically, this is a nested model with $q = 1$. Thus, we can apply Wilks’ theorem to compute the probability that the null hypothesis, that $\theta = \bar{\theta}_1$, is excluded. We then move to the next value of θ , and repeat the operation. The locus of θ values for which we obtain probabilities lower than a threshold α gives the corresponding confidence interval.

Given a sufficiently fine grid of likelihoods, another equivalent option is to directly marginalize the likelihood. However, in general, $\exp(\log \mathcal{L})$ can be a computationally untreatable number. We thus normalize the likelihood to its maximum prior to exponentiating, by computing

$$\bar{\mathcal{L}} = \exp[\log \mathcal{L} - \max \log \mathcal{L}]. \quad (\text{D2})$$

This quantity can then be marginalized, and correctly normalized a posteriori. The contour levels can be obtained as percentiles of the resulting marginalized distribution.

Appendix E












Cross-correlation to Likelihood Mapping by Brogi & Line (2019)













To check the consistency of our method, we retrieved v_{sys} and K_p using the framework described in Brogi & Line (2019), and the best-fitting model computed and scaled as explained in Section 4 and Appendix A. In this scheme, the cross-covariance R between data and the best-fitting model (rather than a binary mask) is computed. As such, the retrieval is model dependent in line with its main application to determine atmospheric properties of exoplanets. Cross-covariance values are translated into log-likelihood via the formula

$$\log(L) = -\frac{N}{2} \log[s_f^2 + s_g^2 - 2R], \quad (\text{E1})$$

where s_f and s_g are the data and model variance, respectively. A Markov chain Monte Carlo is driven by the likelihood in Equation (E1), and run via the Python package `emcee`. Confidence intervals are determined by marginalizing the posterior distributions and computing confidence intervals consistently with the line-weighted binary mask method (see Appendix D). We compared the likelihood distributions for K_p and v_{sys} obtained with the two methods in Figure 3. The frameworks give results consistent at 1σ . The significance of the detection with the framework by Brogi & Line (2019) is 10.3σ , which is higher than the significance found with the line-weighted binary mask case, and the confidence intervals on K_p and v_{sys} are consequently tighter. Possible explanations include (1) the larger amount of pixels and line shape information used in the Brogi & Line (2019) case, and (2) the fact that, in the line-weighted binary mask approach, we do not use a mask tailored to the planetary spectrum but rather a G2 stellar spectrum. A more detailed comparison will be the target of dedicated work.

ORCID iDs

Lorenzo Pino  <https://orcid.org/0000-0002-1321-8856>
 Matteo Brogi  <https://orcid.org/0000-0002-7704-0153>
 Luca Malavolta  <https://orcid.org/0000-0002-6492-2085>
 Michael Line  <https://orcid.org/0000-0002-2338-476X>
 Luca Fossati  <https://orcid.org/0000-0003-4426-9530>
 Aldo Stefano Bonomo  <https://orcid.org/0000-0002-6177-198X>
 Katia Biazzo  <https://orcid.org/0000-0002-1892-2180>
 Ilaria Carleo  <https://orcid.org/0000-0002-0810-3747>
 Elvira Covino  <https://orcid.org/0000-0002-6187-6685>
 Antonino Francesco Lanza  <https://orcid.org/0000-0001-5928-7251>
 Giuseppe Leto  <https://orcid.org/0000-0002-0040-5011>

Antonio Maggio  <https://orcid.org/0000-0001-5154-6108>
 Jesus Maldonado  <https://orcid.org/0000-0002-2218-5689>
 Luigi Mancini  <https://orcid.org/0000-0002-9428-8732>
 Emilio Molinari  <https://orcid.org/0000-0002-1742-7735>
 Isabella Pagano  <https://orcid.org/0000-0001-9573-4928>
 Giampaolo Piotto  <https://orcid.org/0000-0002-9937-6387>
 Ennio Poretti  <https://orcid.org/0000-0003-1200-0473>
 Monica Rainer  <https://orcid.org/0000-0002-8786-2572>
 Alessandro Sozzetti  <https://orcid.org/0000-0002-7504-365X>
 David Ehrenreich  <https://orcid.org/0000-0001-9704-5405>
 Baptiste Lavie  <https://orcid.org/0000-0001-8884-9276>
 Domenico Nardiello  <https://orcid.org/0000-0003-1149-3659>

References

- Arcangeli, J., Désert, J.-M., Line, M. R., et al. 2018, *ApJL*, **855**, L30
 Astropy Collaboration, Price-Whelan, A. M., Sipőcz, B. M., et al. 2018, *AJ*, **156**, 123
 Astropy Collaboration, Robitaille, T. P., Tollerud, E. J., et al. 2013, *A&A*, **558**, A33
 Baranne, A., Mayor, M., & Poncet, J. L. 1979, *VA*, **23**, 279
 Baranne, A., Queloz, D., Mayor, M., et al. 1996, *A&AS*, **119**, 373
 Bard, A., Kock, A., & Kock, M. 1991, *A&A*, **248**, 315
 Bard, A., & Kock, M. 1994, *A&A*, **282**, 1014
 Barklem, P. S., & Aspelund-Johansson, J. 2005, *A&A*, **435**, 373
 Barklem, P. S., & Collet, R. 2016, *A&A*, **588**, A96
 Barklem, P. S., Piskunov, N., & O'Mara, B. J. 2000, *A&AS*, **142**, 467
 Baschek, B., Garz, T., Holweger, H., & Richter, J. 1970, *A&A*, **4**, 229
 Bizzarri, A., Huber, M. C. E., Noels, A., et al. 1993, *A&A*, **273**, 707
 Blackwell, D. E., Shallis, M. J., & Simmons, G. J. 1980, *A&A*, **81**, 340
 Blackwell-Whitehead, R. J., Lundberg, H., Nave, G., et al. 2006, *MNRAS*, **373**, 1603
 Borsa, F., Rainer, M., Bonomo, A. S., et al. 2019, *A&A*, **631**, A34
 Bridges, J. M. 1973, in Eleventh International Conference on Phenomena in Ionized Gases, ed. I. Štoll (Prague: Czechoslovak Acad. of Sciences), 418
 Brogi, M., de Kok, R. J., Albrecht, S., et al. 2016, *ApJ*, **817**, 106
 Brogi, M., & Line, M. R. 2019, *AJ*, **157**, 114
 Brogi, M., Snellen, I. A. G., de Kok, R. J., et al. 2013, *ApJ*, **767**, 27
 Casasayas-Barris, N., Pallé, E., Yan, F., et al. 2019, *A&A*, **628**, A9
 Cash, W. 1976, *A&A*, **52**, 307
 Cauley, P. W., Shkolnik, E. L., Ilyin, I., et al. 2019, *AJ*, **157**, 69
 Claudi, R., Benatti, S., Carleo, I., et al. 2017, *EPJP*, **132**, 364
 Covino, E., Esposito, M., Barbieri, M., et al. 2013, *A&A*, **554**, A28
 Donati, J. F., Semel, M., Carter, B. D., Rees, D. E., & Collier Cameron, A. 1997, *MNRAS*, **291**, 658
 Dumusque, X. 2018, *A&A*, **620**, A47
 Fisher, C., Hoeijmakers, H. J., Kitzmann, D., et al. 2020, *AJ*, **159**, 192
 Fortney, J. J., Lodders, K., Marley, M. S., & Freedman, R. S. 2008, *ApJ*, **678**, 1419
 Fossati, L., Haswell, C. A., Froning, C. S., et al. 2010, *ApJL*, **714**, L222
 Fuhr, J. R., Martin, G. A., & Wiese, W. L. 1988, *JPCRD*, **17**, 4
 Gandhi, S., & Madhusudhan, N. 2019, *MNRAS*, **485**, 5817
 Gaudi, B. S., Stassun, K. G., Collins, K. A., et al. 2017, *Natur*, **546**, 514
 Gibson, N. P., Merritt, S., Nugroho, S. K., et al. 2020, *MNRAS*, **493**, 2215
 Hannaford, P., Lowe, R. M., Grevesse, N., & Noels, A. 1992, *A&A*, **259**, 301
 Haswell, C. A., Fossati, L., Ayres, T., et al. 2012, *ApJ*, **760**, 79
 Helling, C., Gourbin, P., Woitke, P., & Parmentier, V. 2019, *A&A*, **626**, A133
 Hoeijmakers, H. J., Ehrenreich, D., Heng, K., et al. 2018, *Natur*, **560**, 453
 Hoeijmakers, H. J., Ehrenreich, D., Kitzmann, D., et al. 2019, *A&A*, **627**, A165
 Hooton, M. J., Watson, C. A., de Mooij, E. J. W., Gibson, N. P., & Kitzmann, D. 2018, *ApJL*, **869**, L25
 Hubeny, I., Burrows, A., & Sudarsky, D. 2003, *ApJ*, **594**, 1011
 Huser, T. O., Wende-von Berg, S., Dreizler, S., et al. 2013, *A&A*, **553**, A6
 Irwin, P. G. J. 2009, *Giant Planets of Our Solar System* (Berlin: Springer)
 John, T. L. 1988, *A&A*, **193**, 189
 Kitzmann, D., Heng, K., Rimmer, P. B., et al. 2018, *ApJ*, **863**, 183
 Kochukhov, O., Makaganiuk, V., & Piskunov, N. 2010, *A&A*, **524**, A5
 Kroll, S., & Kock, M. 1987, *A&AS*, **67**, 225
 Kupka, F., Piskunov, N., Ryabchikova, T. A., Stempels, H. C., & Weiss, W. W. 1999, *A&AS*, **138**, 119
 Kupka, F. G., Ryabchikova, T. A., Piskunov, N. E., Stempels, H. C., & Weiss, W. W. 2000, *BaltA*, **9**, 590
 Kurucz, R. L. 2010, Robert L. Kurucz On-line Database of Observed and Predicted Atomic Transitions, <http://kurucz.harvard.edu/atoms.html>
 Kurucz, R. L. 2013, Robert L. Kurucz On-line Database of Observed and Predicted Atomic Transitions, <http://kurucz.harvard.edu/atoms.html>
 Kurucz, R. L. 2014, Robert L. Kurucz On-line Database of Observed and Predicted Atomic Transitions, <http://kurucz.harvard.edu/atoms.html>
 Lampton, M., Margon, B., & Bowyer, S. 1976, *ApJ*, **208**, 177
 Lawler, J. E., Guzman, A., Wood, M. P., Sneden, C., & Cowan, J. J. 2013, *ApJS*, **205**, 11
 Liddle, A. R. 2007, *MNRAS*, **377**, L74
 Lothringer, J. D., & Barman, T. 2019, *ApJ*, **876**, 69
 Lothringer, J. D., Barman, T., & Koskinen, T. 2018, *ApJ*, **866**, 27
 Malavolta, L., Lovis, C., Pepe, F., Sneden, C., & Udry, S. 2017, *MNRAS*, **469**, 3965
 Malik, M., Kitzmann, D., Mendonça, J. M., et al. 2019, *AJ*, **157**, 170
 Martin, G., Fuhr, J., & Wiese, W. 1988, *JPCRD*, **17**, 3, <https://www.osti.gov/biblio/6831545-atomic-transition-probabilities-scandium-through-manganese>
 Mollière, P., van Boekel, R., Dullemond, C., Henning, T., & Mordasini, C. 2015, *ApJ*, **813**, 47
 Mollière, P., Wardenier, J. P., van Boekel, R., et al. 2019, *A&A*, **627**, A67
 Nitz, D. E., Wickliffe, M. E., & Lawler, J. E. 1998, *ApJS*, **117**, 313
 Nugroho, S. K., Kawahara, H., Masuda, K., et al. 2017, *AJ*, **154**, 221
 O'Brian, T. R., Wickliffe, M. E., Lawler, J. E., Whaling, W., & Brault, J. W. 1991, *JOSAB*, **8**, 1185
 Parmentier, V., Line, M. R., Bean, J. L., et al. 2018, *A&A*, **617**, A110
 Pauls, U., Grevesse, N., & Huber, M. C. E. 1990, *A&A*, **231**, 536
 Pepe, F., Mayor, M., Galland, F., et al. 2002, *A&A*, **388**, 632
 Pickering, J. C., Thorne, A. P., & Perez, R. 2001, *ApJS*, **132**, 403
 Pino, L., Ehrenreich, D., Allart, R., et al. 2018a, *A&A*, **619**, A3
 Pino, L., Ehrenreich, D., Wyttenbach, A., et al. 2018b, *A&A*, **612**, A53
 Piskunov, N. E., Kupka, F., Ryabchikova, T. A., Weiss, W. W., & Jeffery, C. S. 1995, *A&AS*, **112**, 525
 Raassen, A. J. J., & Uylings, P. H. M. 1998, *A&A*, **340**, 300
 Ryabchikova, T., Piskunov, N., Kurucz, R. L., et al. 2015, *PhysS*, **90**, 054005
 Ryabchikova, T. A., Hill, G. M., Landstreet, J. D., Piskunov, N., & Sigut, T. A. A. 1994, *MNRAS*, **267**, 697
 Ryabchikova, T. A., Piskunov, N. E., Kupka, F., & Weiss, W. W. 1997, *BaltA*, **6**, 244
 Ryabchikova, T. A., Piskunov, N. E., Stempels, H. C., Kupka, F., & Weiss, W. W. 1999, *PhST*, **83**, 162
 Schwarz, H., Brogi, M., de Kok, R., Birkby, J., & Snellen, I. 2015, *A&A*, **576**, A111
 Sharp, C. M., & Burrows, A. 2007, *ApJS*, **168**, 140
 Sing, D. K., Lavvas, P., Ballester, G. E., et al. 2019, *AJ*, **158**, 91
 Snellen, I. A. G., de Kok, R. J., de Mooij, E. J. W., & Albrecht, S. 2010, *Natur*, **465**, 1049
 Sparks, W. B., & Ford, H. C. 2002, *ApJ*, **578**, 543
 Stock, J. W., Kitzmann, D., Patzer, A. B. C., & Sedlmayr, E. 2018, *MNRAS*, **479**, 865
 Thorngren, D., Gao, P., & Fortney, J. J. 2019, *ApJL*, **884**, L6
 Toon, O. B., McKay, C. P., Ackerman, T. P., & Santhanam, K. 1989, *JGR*, **94**, 16287
 Turner, J. D., de Mooij, E. J. W., Jayawardhana, R., et al. 2020, *ApJL*, **888**, L13
 Visscher, C., Lodders, K., & Fegley, B. J. 2010, *ApJ*, **716**, 1060
 Wilks, S. S. 1938, *Ann. Math. Stat.*, **9**, 60
 Wong, I., Shporer, A., Morris, B. M., et al. 2019, arXiv:1910.01607
 Wood, M. P., Lawler, J. E., Sneden, C., & Cowan, J. J. 2013, *ApJS*, **208**, 27
 Yan, F., Casasayas-Barris, N., Molaverdikhani, K., et al. 2019, *A&A*, **632**, A69
 Yan, F., & Henning, T. 2018, *NatAs*, **2**, 714